



High-precision calibration method for shear ratio based on the shearing wavefront feature extraction of a phase plate

RUI ZHANG,¹ YONGYING YANG,^{1,*} ZIJIAN LIANG,¹ JIABIN JIANG,¹ AND TONG LING^{2,3}

¹State Key Laboratory of Modern Optical Instrumentation, College of Optical Science and Engineering, Zhejiang University, Hangzhou 310027, China

²Hansen Experimental Physics Laboratory, Stanford University, Stanford, California 94305, USA

³Department of Ophthalmology, Stanford University, Stanford, California 94305, USA

*Corresponding author: yyyang07@163.com

Received 19 April 2018; revised 24 May 2018; accepted 24 May 2018; posted 30 May 2018 (Doc. ID 328775); published 15 June 2018

A new method based on the shearing wavefront feature extraction (SWFE) of a phase plate is proposed to accurately estimate the shear ratio of the system. The relationship between the shear ratio of a quadriwave lateral shearing interferometer based on a randomly encoded hybrid grating (REHG) and the measurement sensitivity, dynamic range, and wavefront retrieval accuracy is analyzed to provide a theoretical guidance for practical application. The simulation result of the SWFE method shows that the relative error of the shear ratio value is about 1.8×10^{-3} , within the acceptable range of the system. In the experiment, two fused quartz phase plates etched with step change edge grooves were introduced to calibrate the shear ratio of the REHG wavefront diagnosis system. Then, the etching depths of these two phase plates and the figure error of a spherical surface were characterized by the REHG. A comparison with a ZYGO GPI interferometer exhibits that the testing results by the REHG are highly precise, which further confirms the effectiveness of the SWFE method in the shear ratio calibration. This shear ratio calibration method is available for similar kind of shearing interferometric wavefront sensor. ©2018 Optical Society of America

OCIS codes: (120.0120) Instrumentation, measurement, and metrology; (120.3180) Interferometry; (050.1950) Diffraction gratings; (120.5050) Phase measurement.

<https://doi.org/10.1364/AO.57.005121>

1. INTRODUCTION

With rapid development of digital society, aerospace, electronics, military, and other fields put forth higher requirements on optical systems. Optical interferometry provides a sophisticated and effective method for the quality inspection of optical components and systems. As an important branch of interferometry, shearing interferometry has extensive value in research due to its stability, obtained by its self-reference characteristic. As no extra absolute reference flat is required, the system structure of the shearing interferometer is compact and stable [1]. According to the different shearing modes, shearing interferometers are mainly classified as radial shearing interferometers, plane-plate lateral shearing interferometers, and quadriwave lateral shearing interferometers (QWLSIs).

A radial shearing interferometer produces two contracted and expanded wavefronts, generating interferograms in the overlapped area of the two beams—which is widely applied to real-time measurement of high-speed turbulent flow fields

and optical testing [2–4]. The shear ratio of a cyclic radial shearing interferometer is the reciprocal of the magnification of the Galilean telescope system, which is hard to change unless the telescope is substituted. In plane-plate interferometry, a collimated beam is incident on an inclined plane parallel or slightly wedged plate, and is reflected from the front and back of the plate due to Fresnel reflections. The plate thickness introduces a beam displacement, that is, a lateral shear, the amount of which is determined by the thickness of the plate and the beam angle of incidence [5,6]. Two sets of plane-plate shearing systems are often required to obtain shearing wavefront data in two orthogonal directions; this makes the system configuration more complicated and difficult to collimate. QWLSIs are capable of transient phase measurement by acquiring shearing wavefront data in two orthogonal directions simultaneously in a single interferogram. Taking advantage of the compact and common-path features, the QWLSI exhibits great suppression over environmental vibration, and is extensively applied to the field of extreme ultraviolet wavefront metrology [7–9], optical

system aberrations measurement [10,11], and quantitative phase imaging of living cells [12–14].

In our previous work, a novel QWLSI wavefront diagnosis system with strong adaptability and high precision based on a randomly encoded hybrid grating (REHG) has been proposed [15]. Different from a cross-grating lateral shearing interferometer [10] and a QWLSI based on the modified Hartmann mask [16,17], the far-field Fraunhofer diffractions of the REHG contain only +1 and -1 orders in two orthogonal directions, and, thus, no order selection mask is ever needed for the system. Without the influence of the periodical Talbot effect, a continuously variable shear ratio can be obtained with the REHG, which makes it possible to control the dynamic range and measurement sensitivity of the system. Reasonable selection of shear ratio is of crucial importance to the performance of the QWLSI for different specimens under test. To satisfy the Nyquist sampling theorem, a small shear ratio is typically better for large wavefront distortion since the difference between two replicas of the original wavefront with lateral shear is reduced, enlarging the dynamic range of the lateral shearing interferometer [1]. However, a much too small shear ratio will affect the measurement sensitivity and accuracy of the wavefront retrieval. In addition, the shear ratio also has an impact on the effective testing aperture, as the shearing interference only occurs at the overlapped region of the wavefront replicas.

Wavefront retrieval algorithms for QWLSI have been widely discussed in the literature. Whether a modal reconstruction, such as the Rimmer–Wyant method [18] and differential Zernike polynomial fitting (DZF) [19], or zonal reconstruction algorithms [20–22], all need to obtain the shear ratio accurately. Due to the difficulty in precisely determining the relative distance between each component in the actual system, using the principle formula to evaluate the shear ratio will introduce a large error, so as to reduce the wavefront retrieval accuracy. However, a high-precision calibration method for shear ratio in QWLSI is rarely reported in the previous studies.

In this paper, a high-precision shear ratio calibration method based on shearing wavefront feature extraction (SWFE) is proposed, and the influence of shear ratio on the system dynamic range, sensitivity, and wavefront retrieval accuracy is analyzed. A simulation and experiments have been carried out to calibrate the shear ratio based on the SWGE method. Two phase plates etched with step change grooves and a spherical surface figure map are characterized by the REHG and ZYGO GPI, respectively, to validate the accuracy of the shear ratio calibration value.

2. REHG WAVEFRONT DIAGNOSIS SYSTEM

The REHG wavefront diagnosis system can be used in both the transmission mode and reflection mode. The system layout of the collimated beam wavefront diagnosis system in the transmission mode is illustrated schematically in Fig. 1(a). A collimated beam passing through the specimen under test will record the information of the optical surfaces. Once the beam strikes the REHG, it will be diffracted into four identical but tilted replicas of the original wavefront, and then reach the imaging plane to generate a quadriwave lateral shearing interferogram in the overlapped region on the CCD. Figure 1(b) depicts the structure of the phase plate as the specimen. The REHG

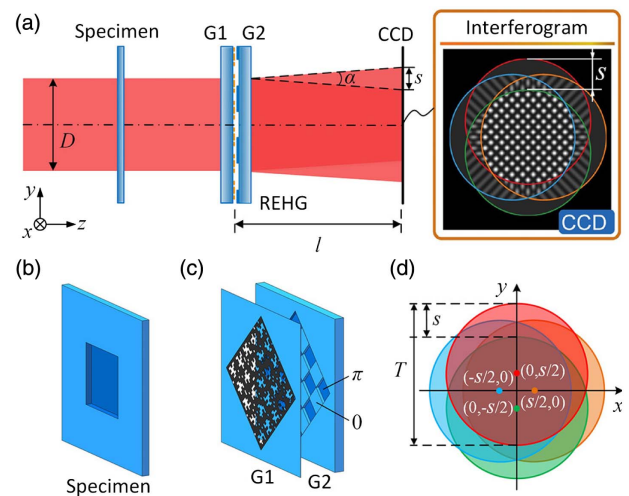


Fig. 1. (a) Layout of the collimated beam wavefront diagnosis system based on the REHG (transmission mode). (b) Schematic diagram of the phase plate. (c) Schematic diagram of the REHG model. (d) Wavefront distribution of four diffraction orders.

consists of a randomly encoded binary amplitude grating marked as G1 and a phase chessboard grating marked as G2 [15]. The randomly encoded binary amplitude grating uses tiny pixels with transmittances of 0 and 1 to simulate the transmission of the ideal quadriwave diffraction grating; however, the phase chessboard is a transparent substrate with a phase gap of π between adjacent grids. If the grid lines of the REHG are placed parallel to the x or y direction, the diffraction beam center of +1 and -1 orders in two orthogonal directions will be located at the angle bisector of x and y axes. For simplicity of deduction, we rotate the REHG by 45° around the optical axis, as presented in Fig. 1(c). Thus, the beam centers will be located at $(s/2, 0)$, $(-s/2, 0)$, $(0, s/2)$, and $(0, -s/2)$ in Cartesian coordinates, as shown in Fig. 1(d). We assume that D is the aperture of the beam, l is the distance between the REHG and the image plane, α is the angle between the wave vectors of the two replicas in x and y directions, s is the shear amount, and T is the beam aperture on the image plane.

In the reflection mode, the optical layout of the spherical surface figure error testing system by the REHG is as shown in Fig. 2. A light beam is converted into a plane wave probe by a collimator consisting of two lenses L_1 and L_2 . Then the probe is transformed into a spherical wave by an aplanatic condenser and hits the spherical mirror. The wavefront carrying the surface figure information of the spherical mirror under test is returned to the beam splitter along the original optical path, and then enters the REHG wavefront diagnosis system to form the interferogram on the image plane of the CCD sensor.

The equivalent grating pitch of the rotated REHG should be multiplied by $\sqrt{2}$ from the original value. According to the diffraction grating equation, the angle $\alpha/2$ satisfies [23,24]

$$\sqrt{2}d \left[\sin\left(\frac{\alpha}{2}\right) - \sin\left(-\frac{\alpha}{2}\right) \right] = 2\lambda, \quad (1)$$

where d is the grating pitch of the REHG. From geometry, we can obtain the following relationship:

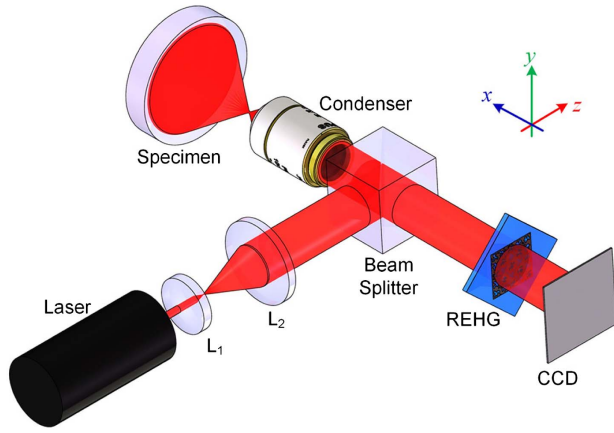


Fig. 2. Layout of the spherical surface testing system based on the REHG (reflection mode).

$$\tan\left(\frac{\alpha}{2}\right) = \frac{s}{2l}. \quad (2)$$

Thus, the shear amount s can be obtained by combining Eqs. (1) and (2):

$$s = 2l \tan\left[\arcsin\left(\frac{\lambda}{\sqrt{2}d}\right)\right]. \quad (3)$$

The beam diameter T on the image plane is equal to the incident beam aperture D for a collimated light testing mode. Thus, the shear ratio of the system can be expressed as

$$\beta = \frac{s}{T} = \frac{2l \tan\left[\arcsin\left(\frac{\lambda}{\sqrt{2}d}\right)\right]}{D}. \quad (4)$$

It can be seen that the shear ratio is determined by the aperture of the beam under test, D , the wavelength λ , the pitch of the REHG, d , and the distance between the grating and the image plane of the CCD, l .

3. METHOD OF REHG INTERFEROGRAM SIMULATION AND WAVEFRONT RETRIEVAL

Different from an interferogram with a fringe pattern in the traditional Twyman–Green and Fizeau interferometric systems, a quadriwave lateral shearing interferogram looks like a collection of dot arrays, as it contains the differential fringes in both x and y directions, just as shown in Fig. 1(a).

To be closer to the actual situation, a mathematical model based on the design principle of a REHG and the Fresnel diffraction theory is introduced to simulate the interferograms when a monochromatic collimated beam is incident onto the system. Figure 3 shows a flowchart of the interferogram simulation and the wavefront retrieval method. First of all, the testing system model illustrated in Fig. 1(a) is built in ZEMAX with an extra figure error of the specimen under test attached artificially, from which we can obtain the distorted wavefront. Let us assume that the coordinate system on the REHG and the image plane are (x_1, y_1) and (x_2, y_2) , respectively. The complex amplitude distribution, $E_1(x_1, y_1)$, remains constant as the collimated beam impinges on the front surface of the REHG, which is given by

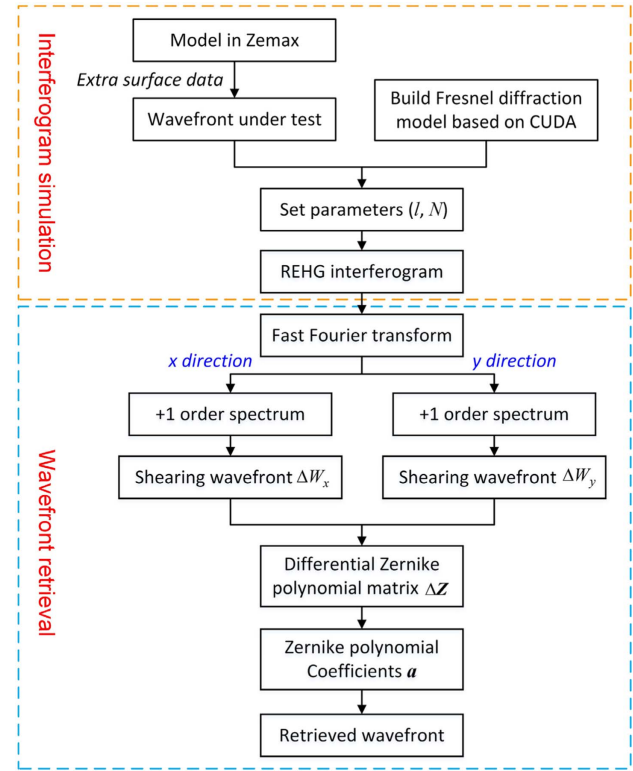


Fig. 3. Flowchart of interferogram simulation and wavefront retrieval of the REHG.

$$E_1(x_1, y_1) = C. \quad (5)$$

Then, the complex amplitude on the rear surface is

$$E'_1(x_1, y_1) = E_1(x_1, y_1) \cdot t(x_1, y_1), \quad (6)$$

where $t(x_1, y_1)$ denotes the complex amplitude transmission coefficient. According to the Fresnel diffraction theory, the complex amplitude $E_2(x_2, y_2)$ on the image plane can be finally obtained:

$$E_2(x_2, y_2) = \frac{\exp(jkl)}{j\lambda l} \cdot A(x_2, y_2), \quad (7)$$

$$A(x_2, y_2) = \iint E'_1(x_1, y_1) \cdot \exp\left\{\frac{jk}{2l}[(x_2 - x_1)^2 + (y_2 - y_1)^2]\right\} dx_1 dy_1. \quad (8)$$

As every point on the image plane needs to execute the double integral mentioned in Eq. (8), the time complexity of this interferogram simulation algorithm is nearly $O(N^4)$ for a single core of CPU with N representing the number of sampling points in one dimension. Actually, as the number of pixels of the REHG will reach thousands, the simulation can be hardly completed within a limited time. Thus, the compute unified device architecture (CUDA) technology developed by NVIDIA is employed to shorten the computation latency from days to seconds. All simulations in this paper are implemented in MATLAB R2017a.

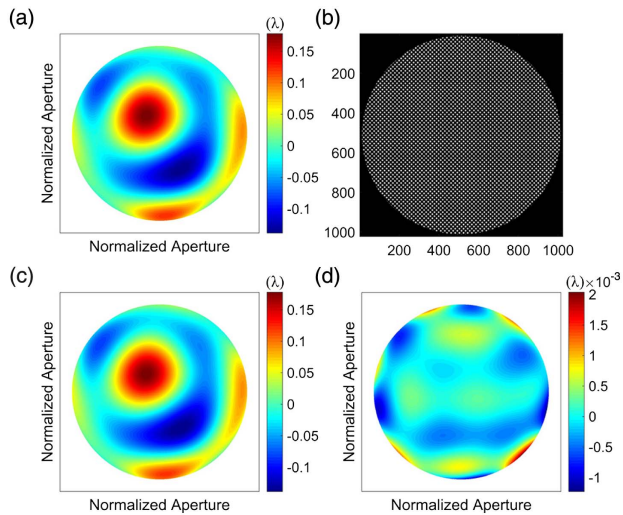


Fig. 4. Simulation results of wavefront retrieval based on the DZF method. (a) Original wavefront. (b) Simulated REHG interferogram. (c) Retrieved wavefront. (d) Residual error between the original and retrieved wavefronts.

In the process of wavefront retrieval, the Fourier spectrum of the interferogram can be obtained by a fast Fourier transform (FFT) first. Then the $+1$ orders in x and y directions of the spectrum are selected by a bandpass filter and transformed into the shearing wavefront by an inverse fast Fourier transform (IFFT), respectively. In the modal wavefront retrieval, the original wavefront under test, $W(x, y)$, can be described by the first N terms of Zernike polynomials in the following form [19]:

$$W(x, y) = \sum_{j=1}^N a_j Z_j(x, y). \quad (9)$$

The shearing wavefront in x and y directions can be written as

$$\left. \begin{aligned} \Delta W_x(x, y) &= W(x - \frac{\xi}{2}, y) - W(x + \frac{\xi}{2}, y) = \sum_{j=1}^N a_j \Delta Z_x \\ \Delta W_y(x, y) &= W(x, y - \frac{\xi}{2}) - W(x, y + \frac{\xi}{2}) = \sum_{j=1}^N a_j \Delta Z_y \end{aligned} \right\}, \quad (10)$$

where

$$\left. \begin{aligned} \Delta Z_x &= Z_j(x - \frac{\xi}{2}, y) - Z_j(x + \frac{\xi}{2}, y) \\ \Delta Z_y &= Z_j(x, y - \frac{\xi}{2}) - Z_j(x, y + \frac{\xi}{2}) \end{aligned} \right\}. \quad (11)$$

In matrix form, Eqs. (10) and (11) can be rewritten as

$$\Delta \mathbf{W} = \Delta \mathbf{Z} \mathbf{a}, \quad (12)$$

where $\Delta \mathbf{W} = (\Delta W_x, \Delta W_y)^T$ and $\Delta \mathbf{Z} = (\Delta Z_x, \Delta Z_y)^T$.

The coefficients \mathbf{a} of the Zernike polynomials can be obtained from the least-square solutions of Eq. (12), that is

$$\mathbf{a} = (\Delta \mathbf{Z}^T \Delta \mathbf{Z})^{-1} \Delta \mathbf{Z}^T \Delta \mathbf{W}. \quad (13)$$

Substituting the coefficients of the Zernike polynomials into Eq. (9), the original wavefront under test can be retrieved finally. The extra figure error data of the specimen are shown in Fig. 4(a), whose peak-to-valley (PV) value is 0.3166 λ and root mean square (RMS) value is 0.0656 λ . The interferogram simulated by the method mentioned above with a shear

ratio of 0.1 is illustrated in Fig. 4(b). Figure 4(c) shows the retrieved wavefront, whereas Fig. 4(d) shows the residual error between the original and the retrieved wavefront with a PV of $3.267 \times 10^{-3} \lambda$ and a RMS of $3.407 \times 10^{-4} \lambda$. We can see that the REHG wavefront diagnosis system combined with the DZF wavefront retrieval algorithm is of high precision for wavefront testing.

4. ANALYSIS OF SHEAR RATIO

A. Relationship between Shear Ratio and Dynamic Range

In the quadriwave lateral shearing interferometric system, the variation of grating pitch not only affects the value of the shear ratio, but also causes a change in the carrier frequency. The relative positions of the 0 order and the $+1$ order in the frequency domain will change accordingly, and the spatial resolution of the retrieved wavefront will be affected eventually. As the image plane should be filled with the interferogram, the aperture of the overlapped region among shearing wavefronts is equal to the size of CCD active area. The wavelength λ , grating pitch d , and the size of the CCD are all fixed during the practical testing process. From Eq. (4), we can see that the shear ratio value is in proportion to the distance l from the grating to the CCD image plane. Thus, the shear ratio of the REHG wavefront diagnosis system can be adjusted easily by changing the distance l .

For lateral shearing interferometry, a large shear ratio is helpful to improve the measurement sensitivity and signal-to-noise ratio (SNR), but is not beneficial for enlarging the dynamic range of the system. To illustrate the issue more clearly, the phase distribution of a wavefront under test is simplified to the situation of a one-dimensional sinusoidal function. As shown in Fig. 5, the blue solid and red dashed-dotted lines indicate, respectively, the original wavefront and its laterally sheared replica. The green dashed line, which is the difference between the blue solid and red dashed-dotted lines, represents the shearing wavefront. The spatial sensitivity of the interferometer will be affected by shot noise [25], but the effect of it is a little difference between the REHG wavefront diagnosis system and the traditional interferometer for the same light source and detector. In this case, the sensitivity is mainly related to the structure of the interference system itself. If the shear ratios are 0.03 and 0.1, then the relative amplitudes of the shearing wavefront and the original wavefront are only 0.188 and 0.618 separately, and the maximum slope of the shearing wavefront is reduced accordingly, as presented in Figs. 5(a) and 5(b), respectively. But if the shear ratio increases to 0.5, as shown in Fig. 5(c), the amplitude of the shearing wavefront will be twice that of the original wavefront; the relative sensitivity can reach its maximum value, whereas the dynamic range is reduced to some extent.

Actually, the wavefront under test always consists of a series of sinusoidal components with different spatial frequencies. According to the Nyquist sampling theorem, each fringe on the image plane of a CCD should occupy at least two pixels to avoid spectrum aliasing. Considering the influence of speckle noise on the interferogram, the maximum slope of the shearing wavefront in x and y directions is generally no more than a quarter of the Nyquist frequency in the simulation and actual

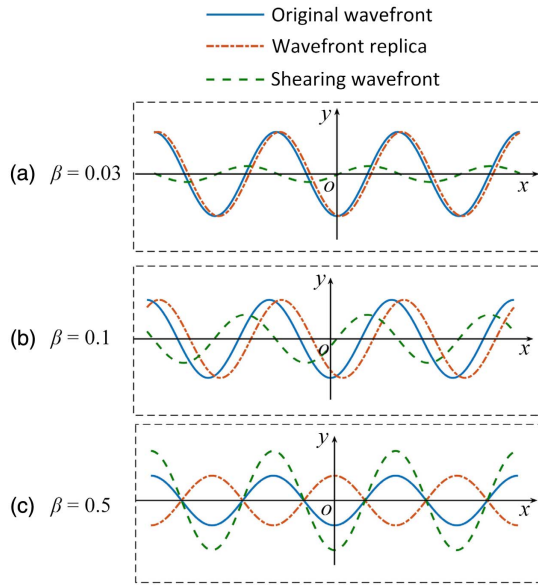


Fig. 5. Lateral shearing schematic diagrams corresponding to different shear ratios of the wavefront under test with one-dimensional sinusoidal phase distribution. (a) $\beta = 0.03$, (b) $\beta = 0.1$, and (c) $\beta = 0.5$.

experiments. That is to say, each fringe occupies at least eight pixels:

$$\left. \begin{aligned} \rho_x &= \frac{\partial(\Delta W_x)}{\partial x} = \partial(W(x - \frac{\xi}{2}, y) - W(x + \frac{\xi}{2}, y)) / \partial x \\ \rho_y &= \frac{\partial(\Delta W_y)}{\partial y} = \partial(W(x, y - \frac{\xi}{2}) - W(x, y + \frac{\xi}{2})) / \partial y \end{aligned} \right\}, \quad (14)$$

$$(\rho_x, \rho_y)_{\max} \leq \frac{1}{4} \rho_0 = 0.125(\lambda/\text{pixel}), \quad (15)$$

where ρ_x and ρ_y represent, respectively, the slopes of the shearing wavefront in x and y directions separately, and ρ_0 is the Nyquist frequency. From Eq. (15), we can see that the concrete value of the dynamic range is determined by the slope of the shearing wavefront in x and y directions. However, different original wavefronts will result in different shearing wavefronts. That is to say, the dynamic range of the system is wavefront-dependent. Suppose the distribution of the wavefront under test is the Peaks function, which is expressed as

$$W = k \cdot [3(1-x)^2 e^{-x^2-(y+1)^2} - 10(x/5 - x^3 - y^5) e^{-x^2-y^2} - e^{-(x+1)^2-y^2}/3], \quad (16)$$

where k is the maximum constant factor according to Eq. (15) for the wavefront under test at different shear ratios. The numerical gradients of the shearing wavefronts in x and y directions can be solved by Eq. (14). Figure 6 shows how the dynamic range and relative sensitivity of the system vary with shear ratio. These analyses provide theoretical guidance for the REHG wavefront diagnosis system to select appropriate shear ratios for different objects to be measured.

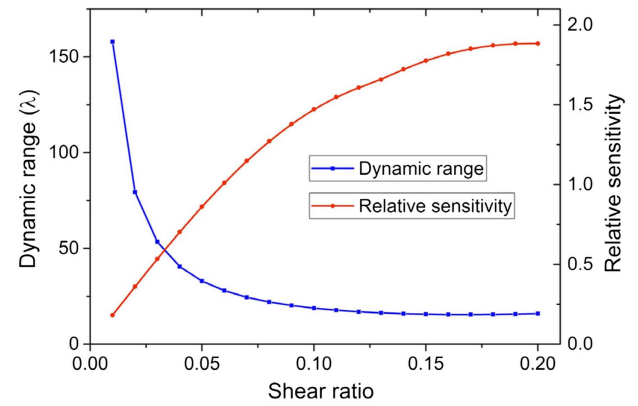


Fig. 6. Variation of the system dynamic range and relative sensitivity with shear ratio.

B. Influence of Shear Ratio on Wavefront Retrieval Precision

As the shear ratio increases, the SNR of the interferogram and the measurement sensitivity also increase within a certain range. With the shear ratio of the system changing from 0.03 to 0.15, the corresponding interferogram is simulated and wavefront retrieval is performed. The residual error curves between the actual figure map and the reconstructed results are shown in Fig. 7(a). It can be seen that residual errors first decrease and then gradually level off and eventually rise again. Considering the effective testing aperture, dynamic range, sensitivity, and wavefront retrieval precision, it is reasonable to set the shear ratio of the REHG below 0.2 in the field of measuring small-scale distorted wavefronts such as optical component figure errors and aberrations.

According to Eqs. (10) and (11), the precision of the shear ratio has a great influence on the accuracy of the wavefront retrieval. It is necessary to discuss the acceptable tolerance range of deviation of the shear ratio from the truth value under the condition that the retrieval precision meets the requirements. The shear ratio is set to 0.05 in the simulation of the interferogram, while a certain error of the shear ratio, Δs , between the calculated and the truth value is attached in the retrieval algorithm. The differential Zernike polynomial changes to

$$\left. \begin{aligned} \Delta Z'_x &= Z_j(x - \frac{s+\Delta s}{2}, y) - Z_j(x + \frac{s+\Delta s}{2}, y) \\ \Delta Z'_y &= Z_j(x, y - \frac{s+\Delta s}{2}) - Z_j(x, y + \frac{s+\Delta s}{2}) \end{aligned} \right\}. \quad (17)$$

As the basis function changes, a certain deviation between the Zernike coefficient and the original value is generated,

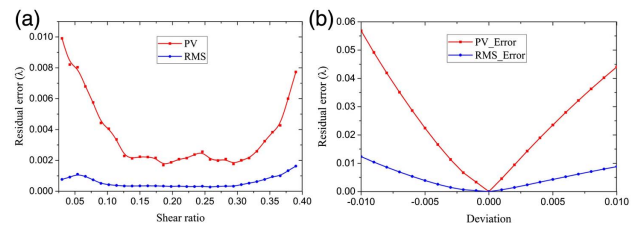


Fig. 7. Simulation results of the effect of system shear ratio on wavefront retrieval precision. (a) Different shear ratios of the system and (b) shear ratio with an error between the calculated value and the true one.

leading to a decrease in the retrieval accuracy. Figure 7(b) shows the simulation results of the residual errors with a maximum shear ratio deviation of 1%. Without considering the systematic errors, the PV value of the residual error is better than $1/100\lambda$ when the shear ratio deviation is controlled to below 3×10^{-3} .

5. SHEAR RATIO CALIBRATION SIMULATION

In the practical testing system, the CCD sensor is protected by always attaching a layer of glass in front of it; the distance between the REHG and the target plane of the CCD, thus, cannot be obtained accurately. If the shear ratio in the retrieval algorithm is calibrated based on Eq. (4), then a large error will be introduced, thereby affecting the wavefront retrieval accuracy. Thus, it is imperative to study a high-precision calibration method for shear ratio.

The information of shear amount is hidden in the shearing wavefront as the wavefront under test is usually a smooth surface with continuous fluctuation just like the one shown in Fig. 4(a). However, if the wavefront contains a shape with sharp step changes such as rectangular grooves, the shear amount can be extracted from the shearing wavefront by means of image processing technology. For this situation, a high-precision calibration method for shear ratio based on the SWFE is proposed, and the optical layout of the simulation is illustrated in Fig. 1(a). A collimated beam passes through a fused quartz phase plate etched with a rectangular groove with a depth of 120 nm as shown in Fig. 8(a); then the wavefront under test enters the REHG wavefront diagnosis system to form a quadriwave lateral shearing interferogram as shown in Fig. 8(b). Figures 8(c) and 8(d) show, respectively, the shearing wavefronts in x and y directions obtained by performing a FFT on the interferogram.

Due to the visible edges of the wavefront under test, the shear amount is reflected in the shearing wavefront intuitively. Digital image processing is performed on the shearing wavefront to extract the edge features in x and y directions, as shown in Figs. 9(a) and 9(b), respectively, from which the shear amount can be obtained. As depicted in the rectangular shaded box in Fig. 8, n sets of sampling points in the middle of the edge features are selected for calculation to avoid a relatively large error at the corner of the shearing wavefront during edge extraction. The shear amounts in x and y directions can be expressed, respectively, as

$$\left. \begin{aligned} s_x &= \frac{1}{n} \sum_{i=1}^n \frac{(x_{2i}-x_{1i})+(x_{4i}-x_{3i})}{2} \\ s_y &= \frac{1}{n} \sum_{j=1}^n \frac{(y_{2j}-y_{1j})+(y_{4j}-y_{3j})}{2} \end{aligned} \right\}, \quad (18)$$

where $x_{1i}, x_{2i}, x_{3i}, x_{4i}$ are the abscissa values of the i th sampling points in the x -direction shearing wavefront, and $y_{1j}, y_{2j}, y_{3j}, y_{4j}$ are the ordinate values of the j th sampling points in the y -direction shearing wavefront. According to the design principle of the REHG, these two shear amounts, s_x and s_y , are of the same value. To reduce the calibration error, the shear amount of the system, s , is described as

$$s = (s_x + s_y)/2. \quad (19)$$

When the shear ratio of the system in the simulation is set to 0.1, the calculated shear amount based on the SWFE is 52.045

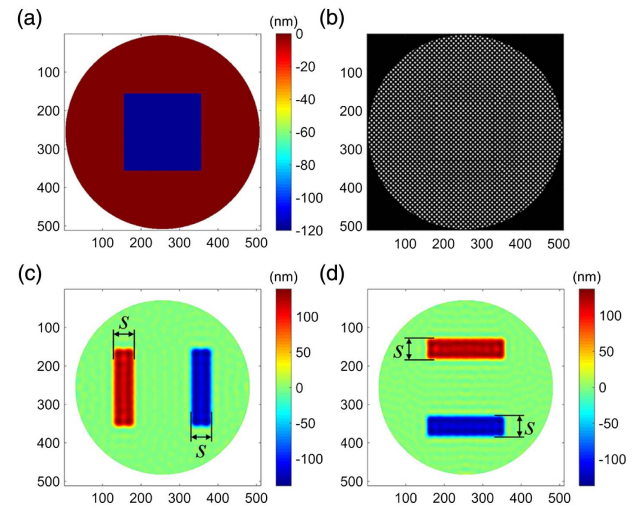


Fig. 8. Shear ratio calibration simulation. (a) Original wavefront under test. (b) Simulated interferogram of the REHG. (c) Shearing wavefront in x direction. (d) Shearing wavefront in y direction.

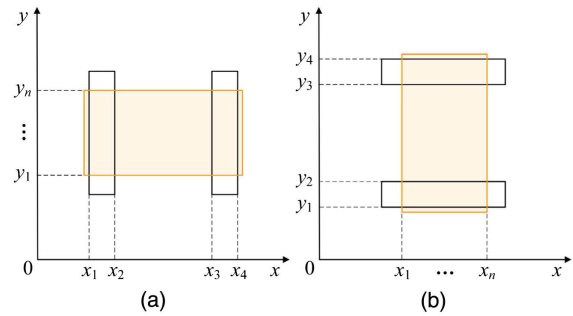


Fig. 9. Diagram of edge feature extraction. (a) Edge feature of the x -direction shearing wavefront and (b) edge feature of the y -direction shearing wavefront.

pixels with a full beam aperture of 511 pixels. Thus, the value of shear ratio is 0.1018 and the deviation from the theoretical value is 1.8×10^{-3} , within the acceptable error range of the previous analysis. As the etching pattern of the phase plate has a sharp step change edge rather than a smooth continuous distribution, a large retrieval error will be generated by the DZF algorithm with finite terms [22]. Thus, the zonal reconstruction algorithm based on the least-square method should be employed to further characterize the etching depth of the phase plate.

6. SYSTEMATIC ERROR CONTROL

Due to the common-path and self-reference characteristics, the REHG wavefront diagnosis system is of great anti-interference ability and high repeatability in practical measurement if the shear ratio is well calibrated. But aberration and misalignment of the components, an extra wavefront aberration of the REHG, and a tilt error of the CCD image plane in the optical alignment process will be inevitably introduced into the testing result. If, however, the calibration precision of the shear ratio is verified by the wavefront measurement accuracy, the

influence of systematic error on the testing result should be eliminated [26,27].

Suppose that the systematic error is W_e ; the testing result of the wavefront by the REHG is W_t ; the actual wavefront distortion of the phase plate is W_p ; and the figure error of the spherical mirror under test is W_s . In the transmission mode, the systematic error W_e can be obtained from the testing result by the REHG without the phase plate in the system. The actual wavefront distortion of the phase plate, W_p , can be expressed as

$$W_p = W_t - W_e. \quad (20)$$

In the reflection mode, the wavefront distortion under test, W_f , is completely determined by the systematic error W_e regardless of the figure distribution of the mirror under test when it is located at the focal plane of the aplanatic condenser; that is

$$W_f = W_e. \quad (21)$$

The figure error of the spherical mirror under test, W_s , can be described as

$$W_s = W_t - W_f. \quad (22)$$

7. EXPERIMENT RESULTS

Experiments are carried out to calibrate the shear ratio of the REHG based on the SWFE of two phase plates etched with different pattern grooves. Comparisons of the testing results of these two phase plates and a spherical surface obtained by the REHG and ZYGO GPI are made to verify the accuracy of the shear ratio calibration value.

A. Shear Ratio Calibration Based on the SWFE

The optical system of the shear ratio experiment has been established based on the layout sketched in Fig. 1(a). The wavefront under test was diffracted into four replicas by the REHG, and a quadriwave lateral shearing interferogram with a pixel size of 2056×2056 was generated on the CCD image plane. The pitch of the REHG was designed to be $60 \mu\text{m}$ in consideration of the spatial resolution of the final measurement results and the fabrication complexity of the grating. Without the zeros padding in the frequency domain in the process of IFFT, the spatial resolution of the testing results can reach 361×361 pixels.

To mitigate speckle noise and distortions resulting from parasitic reflections inside the optical setup [28], a partially coherent LED light source with a center wavelength of 623 nm and a spectral full width at half-maximum of 18 nm was implemented in the system. Two fused quartz phase plates etched with grooves with a maximum size of $4 \text{ mm} \times 4 \text{ mm}$ were utilized in the experiment to calibrate the shear ratio precisely. Of these plates, the one etched with a square groove is recorded as phase plate 1, whereas the other one, etched with a dual square-shaped groove, is recorded as phase plate 2. The interferograms of these two phase plates are shown in Figs. 10(a1) and 10(b1). To display the figure more clearly, partially enlarged details of the center spots are shown in a red box at the top right corner of each interferogram. By performing the Fourier transform spatial phase demodulation method, the shearing wavefront in x and y directions of these two phase plates can be obtained, as shown in Figs. 10(a2), 10(a3), 10(b2), and 10(b3). The shear

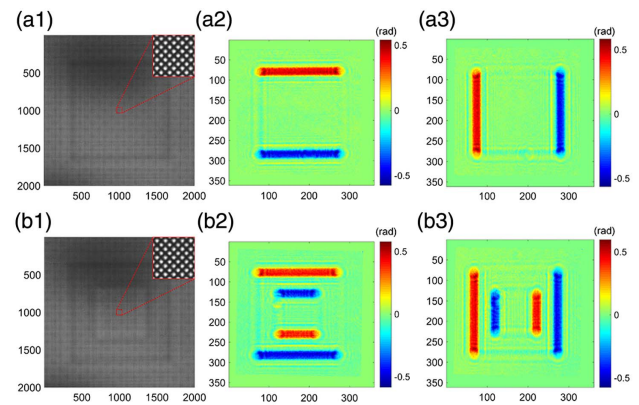


Fig. 10. Experiment results of shear ratio calibration. (a1) Interferogram of phase plate 1 etched with a rectangular groove. (a2) Shearing wavefront in x direction of phase plate 1. (a3) Shearing wavefront in y direction of phase plate 1. (b1) Interferogram of phase plate 2 etched with a rectangular annulus groove. (b2) Shearing wavefront in x direction of phase plate 2. (b3) Shearing wavefront in y direction of phase plate 2.

amounts calculated from the shearing wavefront of these two phase plates are 16.534 pixels and 16.678 pixels, and the corresponding shear ratios are 0.0458 and 0.0462, respectively. It can be seen that the results of the shear ratio calibration of the REHG by the two phase plates etched with different groove patterns are nearly the same, indicating the consistency of the SWFE method.

B. Validation of the Shear Ratio Calibration Method

To illustrate the accuracy of the shear ratio calibration, the etching depths of these two phase plates were characterized; the measurement results were compared with the results obtained with the ZYGO GPI, by which the optical path difference (OPD) has been converted to the etching depths of the grooves (Fig. 11). Figures 11(a1) and 11(b1) depict the testing results of phase plate 1 and 2 by the REHG, and the corresponding 3D visualizations are shown in Figs. 11(a2) and 11(b2), respectively. For comparison, the testing results of the same two phase plates obtained with the ZYGO GPI are presented in Figs. 11(a3) and 11(b3). The detailed one-dimensional distributions of etching depth along the central position of these two phase plates—marked with white dashed lines in Figs. 11(a1) and 11(b1)—are plotted in Figs. 11(a4) and 11(b4), respectively. The results of OPD have been converted into the etching depths of the grooves. The RMS deviations of the two phase plates between the REHG and the ZYGO GPI are 6.173 and 5.162 nm, respectively, which exhibits high precision of the shear ratio calibration value.

As shown in Fig. 9, an experimental spherical surface measurement system has been set up to further verify the validity of the proposed method for shear ratio calibration. As the optical layout of the shear ratio calibration experiment is a transmission system, the energy loss of a light beam is negligible. However, the spherical surface measurement is a reflection system, in which a light beam enters the REHG wavefront sensor with significant energy loss after multiple reflections by the beam splitter and spherical mirror. Limited by the photosensitivity

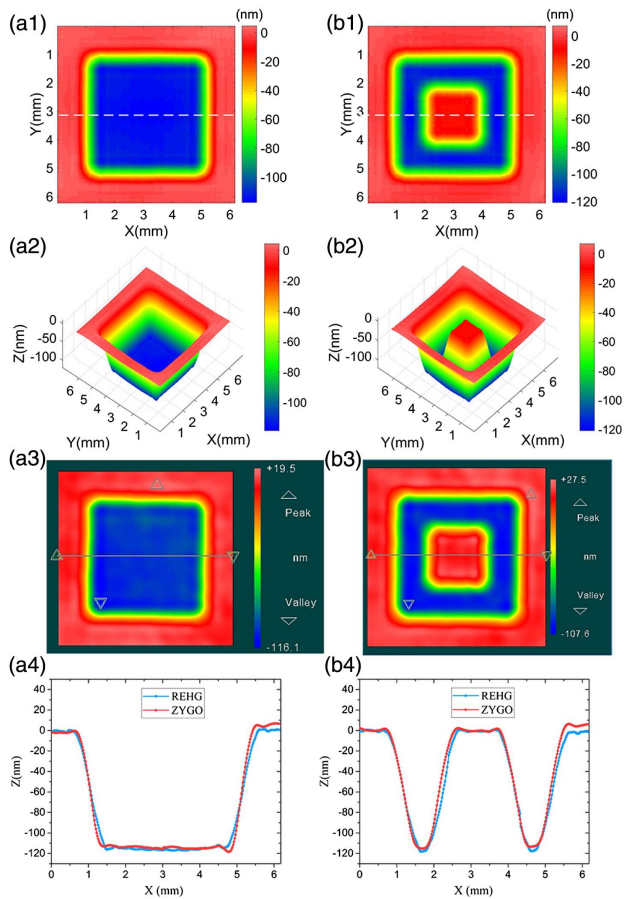


Fig. 11. Comparative experiment results obtained with a ZYGO GPI interferometer. Panels (a1) and (b1) show, respectively, the etching depth distributions of phase plate 1 and phase plate 2 as measured by the REHG. Panels (a2) and (b2) show, respectively, the 3D phase visualizations of phase plate 1 and phase plate 2. Panels (a3) and (b3) show, respectively, the testing results of phase plate 1 and phase plate 2 obtained with a ZYGO GPI interferometer. Panels (a4) and (b4) show, respectively, the profiles of etching depth distribution in x direction along the central position of phase plate 1 and phase plate 2.

of the sensor of the CCD, the contrast of the interferogram will be very poor if the LED is selected as the light source. Therefore, a He-Ne laser with a wavelength of 632.8 nm was applied to the spherical surface figure error measurement system.

First, a spherical mirror with a diameter of 50.8 mm and a radius of curvature of 200 mm was placed at the focal plane of the aplanatic condenser to calibrate the systematic errors. Then, a spherical mirror with a five-axis adjustable mount for optical alignment was placed in the confocal position of the aplanatic condenser to test the distribution of its figure error. The interferograms of these two procedures are shown in Figs. 12(a) and 12(b). With the systematic errors removed, the figure error of the spherical mirror can be retrieved accurately by the REHG, as depicted in Fig. 12(c). Figure 12(d) is the test result of the same spherical mirror by the ZYGO GPI interferometer. Table 1 presents multiple repeated experiments; the average PV and RMS values of the test results by the REHG are 0.182λ and 0.045λ , whereas the average PV and RMS

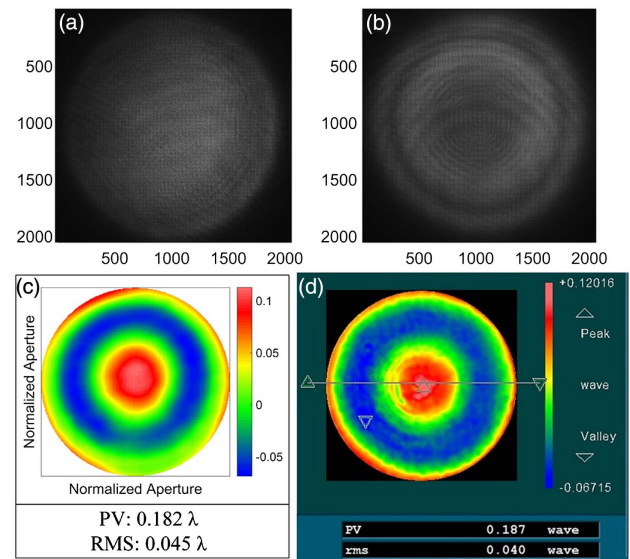


Fig. 12. Measurement results of the surface figure error of the spherical mirror. Panels (a) and (b) show, respectively, the interferograms of the spherical mirror under test located at the focal point and the confocal position of the aplanatic condenser. (c) Figure error retrieved by the REHG. (d) The testing result of the same spherical mirror obtained with a ZYGO GPI.

Table 1. Comparative Results of the Spherical Mirror's Figure Error between the REHG and the ZYGO GPI

	1	2	3	Average
REHG				
PV (λ)	0.182	0.184	0.181	0.182
RMS (λ)	0.045	0.045	0.045	0.045
ZYGO GPI				
PV (λ)	0.187	0.192	0.191	0.190
RMS (λ)	0.040	0.040	0.040	0.040

with the ZYGO GPI interferometer are 0.190λ and 0.040λ , respectively. The comparison results show that the REHG wavefront sensor exhibits both high precision and high repeatability, which also demonstrate the accuracy of the shear ratio calibration.

8. CONCLUSION

Reasonable selection and accurate calibration of shear ratio play a crucial role in a quadriwave lateral shearing interferometric system. As a practical matter, the distance between the REHG and the CCD sensor is difficult to obtain accurately. A large error will be inevitably introduced, if the shear ratio is evaluated by the principle formula. The accuracy of wavefront retrieval will be seriously affected if the shear ratio deviates from the truth value, although a high-precision calibration method for shear ratio in QWLSI is rarely reported in previous studies. In this paper, a high-precision shear ratio calibration method based on the SWFE is proposed, and the influence of shear ratio on the system's dynamic range, sensitivity, and

wavefront retrieval accuracy is analyzed. To be closer to practical application, with the help of the CUDA technology, a mathematical model based on the design principle of a REHG and the Fresnel diffraction theory is introduced to simulate the interferogram. Simulation results have demonstrated the feasibility of the SWFE method. A comparison with the ZYGO GPI interferometer exhibits that the wavefront testing result by the REHG is highly precise and also shows good repeatability, which reveals the accuracy of the shear ratio calibration. The QWLSI based on a REHG with an accurately calibrated shear ratio shows features of high precision, high resolution, good repeatability, and strong anti-interference ability, and has extensive application prospects in optics surface testing, quantitative phase imaging, and other fields.

Funding. National Natural Science Foundation of China (NSFC) (61627825); State Key Laboratory of Modern Optical Instrumentation Innovation Program (MOI2015 B06); Zhejiang University.

REFERENCES

1. D. Malacara, *Optical Shop Testing*, 3rd ed. (2006), pp. 46–96.
2. T. Ling, D. Liu, Y. Yang, L. Sun, C. Tian, and Y. Shen, "Off-axis cyclic radial shearing interferometer for measurement of centrally blocked transient wavefront," *Opt. Lett.* **38**, 2493–2495 (2013).
3. N. T. Gu, L. H. Huang, Z. P. Yang, Q. Luo, and C. H. Rao, "Modal wavefront reconstruction for radial shearing interferometer with lateral shear," *Opt. Lett.* **36**, 3693–3695 (2011).
4. N. Gu, B. Yao, L. Huang, and C. Rao, "Compact single-shot radial shearing interferometer with random phase shift," *Opt. Lett.* **42**, 3622–3625 (2017).
5. X. Dai, X. Shao, L. Li, C. Liu, M. Dai, H. Yun, and F. Yang, "Shape measurement with modified phase-shift lateral shearing interferometry illumination and radial basis function," *Appl. Opt.* **56**, 5954–5960 (2017).
6. X. Liu, Y. Gao, and M. Chang, "A new lateral shearing interferometer for precision surface measurement," *Opt. Lasers Eng.* **47**, 926–934 (2009).
7. A. M. Khounsary, M. Hasegawa, C. Ouchi, T. Hasegawa, S. Kato, A. Ohkubo, A. Suzuki, K. Sugisaki, M. Okada, K. Otaki, K. Murakami, J. Saito, M. Niibe, M. Takeda, U. Dinger, and K. Ota, "Recent progress of EUV wavefront metrology in EUVA," *Proc. SPIE* **5533**, 27–36 (2004).
8. R. S. Mackay, S. Kato, C. Ouchi, M. Hasegawa, A. Suzuki, T. Hasegawa, K. Sugisaki, M. Okada, Y. Zhu, K. Murakami, J. Saito, M. Niibe, and M. Takeda, "Comparison of EUV interferometry methods in EUVA project," *Proc. SPIE* **5751**, 110–117 (2005).
9. R. M. Silver, Y. Zhu, K. Sugisaki, M. Okada, K. Otaki, Z. Liu, M. Ishii, J. Kawakami, J. Saito, K. Murakami, C. Ouchi, M. Hasegawa, S. Kato, T. Hasegawa, A. Suzuki, and M. Niibe, "Experimental comparison of absolute PDI and lateral shearing interferometer," *Proc. SPIE* **5752**, 1192–1199 (2005).
10. T. Ling, Y. Yang, X. Yue, D. Liu, Y. Ma, J. Bai, and K. Wang, "Common-path and compact wavefront diagnosis system based on cross grating lateral shearing interferometer," *Appl. Opt.* **53**, 7144–7152 (2014).
11. T. Ling, Y. Y. Yang, D. Liu, X. M. Yue, J. B. Jiang, J. Bai, and Y. B. Shen, "General measurement of optical system aberrations with a continuously variable lateral shear ratio by a randomly encoded hybrid grating," *Appl. Opt.* **54**, 8913–8920 (2015).
12. P. Bon, G. Maucort, B. Wattellier, and S. Monneret, "Quadriwave lateral shearing interferometry for quantitative phase microscopy of living cells," *Opt. Express* **17**, 13080–13094 (2009).
13. P. Bon, B. Wattellier, and S. Monneret, "Modeling quantitative phase image formation under tilted illuminations," *Opt. Lett.* **37**, 1718–1720 (2012).
14. T. Ling, J. Jiang, R. Zhang, and Y. Yang, "Quadriwave lateral shearing interferometric microscopy with wideband sensitivity enhancement for quantitative phase imaging in real time," *Sci. Rep.* **7**, 9 (2017).
15. T. Ling, D. Liu, X. Yue, Y. Yang, Y. Shen, and J. Bai, "Quadriwave lateral shearing interferometer based on a randomly encoded hybrid grating," *Opt. Lett.* **40**, 2245–2248 (2015).
16. J. Primot and N. Guerineau, "Extended Hartmann test based on the pseudoguiding property of a Hartmann mask completed by a phase chessboard," *Appl. Opt.* **39**, 5715–5720 (2000).
17. S. Mousset, C. Rouyer, G. Marre, N. Blanchot, S. Montant, and B. Wattellier, "Piston measurement by quadriwave lateral shearing interferometry," *Opt. Lett.* **31**, 2634–2636 (2006).
18. W. Shen, M. W. Chang, and D. S. Wan, "Zernike polynomial fitting of lateral shearing interferometry," *Opt. Eng.* **36**, 905–913 (1997).
19. F. Dai, F. Tang, X. Wang, O. Sasaki, and P. Feng, "Modal wavefront reconstruction based on Zernike polynomials for lateral shearing interferometry: comparisons of existing algorithms," *Appl. Opt.* **51**, 5028–5037 (2012).
20. S. Velghe, J. Primot, N. Guerineau, M. Cohen, and B. Wattellier, "Wave-front reconstruction from multidirectional phase derivatives generated by multilateral shearing interferometers," *Opt. Lett.* **30**, 245–247 (2005).
21. F. Dai, F. Tang, X. Wang, and O. Sasaki, "Generalized zonal wavefront reconstruction for high spatial resolution in lateral shearing interferometry," *J. Opt. Soc. Am. A* **29**, 2038–2047 (2012).
22. T. Ling, Y. Y. Yang, D. Liu, X. M. Yue, and J. B. Jiang, "Retrieval of phase distributions from the quadriwave lateral shearing interferogram obtained by randomly encoded hybrid grating," *Proc. SPIE* **9633**, 96332G (2015).
23. J. C. Chanteloup, "Multiple-wave lateral shearing interferometry for wave-front sensing," *Appl. Opt.* **44**, 1559–1571 (2005).
24. M. Born and E. Wolf, *Principles of Optics* (Cambridge University, 1999), Vol. 1, p. 986.
25. P. Hosseini, R. Zhou, Y. H. Kim, C. Peres, A. Diaspro, C. Kuang, Z. Yaqoob, and P. T. So, "Pushing phase and amplitude sensitivity limits in interferometric microscopy," *Opt. Lett.* **41**, 1656–1659 (2016).
26. W. Zhu, J. Li, L. Chen, D. Zheng, Y. Yang, and Z. Han, "Systematic error analysis and correction in quadriwave lateral shearing interferometer," *Opt. Commun.* **380**, 214–220 (2016).
27. D. Wang, Y. Xu, R. Liang, M. Kong, J. Zhao, B. Zhang, and W. Li, "High-precision method for submicron-aperture fiber point-diffraction wavefront measurement," *Opt. Express* **24**, 7079–7090 (2016).
28. J. A. Rodrigo and T. Alieva, "Rapid quantitative phase imaging for partially coherent light microscopy," *Opt. Express* **22**, 13472–13483 (2014).